



OPEN

# Helical model of compression and thermal expansion

Sylwia Zięba<sup>1✉</sup>, Michalina Rusek<sup>2</sup>, Andrzej Katrusiak<sup>2</sup>, Andrzej Gzella<sup>3</sup>, Alina T. Dubis<sup>4</sup> & Andrzej Łapiński<sup>1✉</sup>

A negative linear temperature expansion and a negative linear compressibility were observed for imidazolium benzoate salt. Its strongly anisotropic strain induced by the temperature and pressure changes has been explained by the mechanism of H-bonded helices deformed in the structure. X-ray diffraction and vibrational spectroscopy were used to analyze interactions in the crystal. The Quantum Theory of Atoms in Molecules (QTAIM) approach was applied to analyze the hydrogen bonds and other interactions. In the salt under study, the interactions within the helix are substantially higher in energy than between helices. With decreasing temperature and increasing pressure, the value of the helix pitch increases while the value of the semi-major axis decreases, which results in the negative linear expansion and negative linear compression, respectively.

Negative linear compressibility (NLC) and negative area compressibility (NAC) are rare types of crystal strain in which one or two dimensions expand with increasing hydrostatic pressure<sup>1–3</sup>. In general, NLC is much weaker than conventional materials' typical positive compressibility<sup>4</sup>. Materials that exhibit negative linear compressibility can be used to build, for example, pressure sensors, artificial muscles, or actuators<sup>4</sup>. In most crystals, their dimensions changes are monotonic<sup>5</sup>. Negative thermal expansion (NTE) can also occur in materials where NLC is observed<sup>6,7</sup>. The NTE is a phenomenon in which one, two or three dimensions reduce with increasing temperature<sup>6</sup>. The phenomenon of negative and zero temperature expansion can find application, for example, in thermomechanical sensors, actuators, precision optical mirrors, fiber optic systems, packaging materials for meshes with the suitable light coefficient, high-performance explosive sensors<sup>1,3,8,9</sup>.

Negative temperature expansion can occur in crystals along one, two, or three principal axes. Negative temperature expansion in one direction has been observed in such crystals as 2,6-dimethylaniline monohydrate (BTA-DMA-H<sub>2</sub>O)<sup>10</sup>, nitromethane solvate 18-crown-6<sup>11</sup>, hydrated tryptophylglycine dipeptide (TrpGly-H<sub>2</sub>O)<sup>12</sup>. We can also distinguish a group of crystals in which NTE occurs in two directions: (S,S)-octa-3,5-diyne-2,7-diol<sup>13</sup>, 2,4-dinitroanisole<sup>14</sup>. There is also a group of materials with volumetric negative temperature expansion: Y<sub>2</sub>Mo<sub>3</sub>O<sub>12</sub><sup>15</sup>, and M<sup>II</sup>Pt<sup>IV</sup>(CN)<sub>6-x</sub>{H<sub>2</sub>O}<sup>16</sup>. There is also a small group of compounds in which we observe near-zero temperature expansion: YbGaGe<sup>17</sup>, (1-x)PbTiO<sub>3-x</sub>Bi(Mg, Ti)<sub>1/2</sub>O<sub>3</sub><sup>18</sup>. One way to obtain such materials is to synthesize them from a mixture of compounds exhibiting PTE and NTE<sup>17</sup>. Very rarely are combinations of PTE, NTE, and ZTE in the same material<sup>19</sup>. Such a situation is explained by the “stretching-tilting mechanism”, “hinge mechanism”, or “lattice fence mechanism”<sup>20,21</sup>.

In the literature, however, no single mechanism explains the nature of the NTE phenomenon. From time to time, there are reports describing the explanation of the origin of the anomalous behavior of the material by various mechanisms: e.g., the “transverse vibration” effect<sup>8,22,23</sup>, “scissors” effect<sup>24</sup>, “accordion motion”<sup>25</sup>, “the sliding of layers”<sup>10,25</sup>, “jack motion”<sup>26</sup>, “fencing mechanism”<sup>13,21</sup>, “pedal-wheel motion”<sup>27</sup>. Recently, Cairns and Goodwin<sup>4</sup> grouped materials exhibiting NLC into four groups depending on the microscopic mechanism responsible for NLC: (a) compounds in which NLC is a consequence of ferroelectric phase transitions, (b) network solids for which correlated polyhedral tilts drive NLC, (c) helical systems, and (c) framework materials with wine-rack, honeycomb, or related topologies, where NLC arises from framework hinging. Ferroelastic instabilities are exhibited by rutile, in which ferroelectric instability is due to the rotation of neighboring columns of octahedra<sup>28</sup>, and zinc cyanide, with symmetry-breaking mechanisms, such as a phonon instability<sup>29</sup>. Polyhedral tilting has been observed in the nonlinear optical (NLO) material BiB<sub>3</sub>O<sub>6</sub>; the dominant deformation mechanism under hydrostatic pressure involves correlated tilting of BO<sub>3</sub> units, which act to hinge the connected borate framework<sup>30</sup>. The most likely mechanism responsible for NLC in the system would involve PO<sub>4</sub> rotation-driven collapse of the

<sup>1</sup>Institute of Molecular Physics, Polish Academy of Sciences, Smoluchowskiego 17, 60-179 Poznan, Poland. <sup>2</sup>Faculty of Chemistry, Adam Mickiewicz University, Uniwersytetu Poznańskiego 8, 61-614 Poznan, Poland. <sup>3</sup>Department of Organic Chemistry, Poznan University of Medical Sciences, Grunwaldzka 6, 60-780 Poznan, Poland. <sup>4</sup>Faculty of Chemistry, University of Białystok, Ciołkowskiego 1K, 15-245 Białystok, Poland. ✉email: sylwia.zieba@ifmpan.poznan.pl; lapinski@ifmpan.poznan.pl

herringbone hydrogen-bonding network<sup>31</sup>. The helix, responsible for NLC, was observed in trigonal polymorphs of elemental selenium and tellurium<sup>32</sup>. A molecular framework mechanism has been described for silver(I) hexacyanocobaltate(III),  $\text{Ag}_3[\text{Co}(\text{CN})_6]$ <sup>6</sup>.

In the compounds derived from carboxylic acids and heterocyclic molecules, anomalous temperature expansion<sup>10,20,33</sup> and negative linear compressibility<sup>7</sup> were observed. In compounds with negative temperature expansion, negative pressure expansion often occurs<sup>5,7</sup>. A change in pressure from 0.2 to 0.5 GPa causes similar changes in crystal volume as a reduction in temperature from 300 to 100 K<sup>34</sup>. The effects of increased pressure are similar to those observed under conditions of lowering the temperature for organic and metal–organic crystals<sup>35</sup>. As early as the 1980s, it was pointed out that hydrogen bonds can affect the occurrence of anomalous temperature expansion and negative linear compressibility<sup>31</sup>.

The authors of this paper have studied the physicochemical properties of compounds derived from carboxylic acids and heterocyclic molecules<sup>19,36,37</sup>. The attraction of this group of materials lies in the fact that the physical properties are influenced by the hydrogen bonding network in these salts<sup>10,38</sup>. By appropriately selecting substrates in the synthesis, we can control the amount and strength of hydrogen bonds. Our previous structural and spectroscopic studies carried out for (bis)imidazolium terephthalate<sup>19</sup> showed the occurrence of negative temperature expansion phenomena, which is associated with the  $\text{N}^+-\text{H}\cdots\text{O}^-$  hydrogen bond network.

The phenomenon of negative temperature expansion was also observed for organic compounds with helix-forming hydrogen bonds: (*S,S*)-octa-3,5-diyne-2,7-diol<sup>13</sup> and (bis)imidazolium terephthalate<sup>19</sup>. As early as the 1970s, attempts were made to link the occurrence of the helix motif to the phenomenon of negative linear compressibility<sup>32</sup>. From the literature, we know several ring molecules based on which the helical structure was obtained, such as (7)phenylene<sup>39</sup>, oligoamides<sup>39</sup>, or tetrakis(7)helicene<sup>40</sup>. Intramolecular and intermolecular hydrogen bonds play a stabilizing role and influence the organization of molecules in the helix<sup>39</sup>. The type and shape of the helix are influenced by the substituents attached to the aromatic ring and  $\pi-\pi$  interactions<sup>39,40</sup>. Molecules forming a helical structure are distinguished by hydrogen bonding ability, chirality, hydrophilicity, or hydrophobicity<sup>41</sup>.

In the above work, we propose a helical model, to our knowledge not previously found in the literature, to explain the crystal's anomalous temperature and pressure behavior. For structural and spectroscopic studies, we chose imidazolium benzoate salt (**BenImi**)<sup>37</sup>, for which a helical structure formed by ions connected by hydrogen bonds  $\text{N}^+-\text{H}\cdots\text{O}^-$  is observed.

## Results and discussion

On the basis of X-ray analysis, it was determined that the **BenImi** compound is imidazolium benzoate (formula moiety:  $\text{C}_7\text{H}_5\text{O}_2^-$ ,  $\text{C}_3\text{H}_5\text{N}_2^+$ ) (Fig. S1), crystallizing in a monoclinic system and space group  $P2_1/n$  (Tables S1 and S2). The asymmetric part of the unit cell is composed of one anion and one cation molecule.

Analysis of the crystal's structure revealed that the molecules of imidazolium cation and benzoate anion, related by 2<sub>1</sub> axis, are connected by hydrogen bonds  $\text{N1a}-\text{H1a}\cdots\text{O9b}$  and  $\text{N2a}-\text{H2a}\cdots\text{O8b}^i$  into helix-shaped chains (Fig. 1). Neighboring antiparallel chains are further connected by hydrogen bonds  $\text{C1a}-\text{H1a}\cdots\text{O9b}^{ii}$  into beta-harmonic layers parallel to the (101) plane (Tables S3 and S4, Fig. S2). Analysis of the layer's structure showed that the molecules of the benzoate anion form its outer shell, while the molecules of the imidazolium cation form the inner ribbing (Fig. S2). Interactions  $\text{C}-\text{H}\cdots\text{Cg1}^{iii}$  were noted between the layers (Fig. S2).

At various temperatures (100, 130, 180, 240, 300 K), X-ray analyses on crystals of imidazolium benzoate were conducted. They demonstrated the stability of the crystal structure in the temperature above range, especially the invariability of its symmetry (vide supra). The situation differs for the unit cell parameters *a*, *b*, *c*, and  $\beta$  angle, which undergo observable changes (Table S5). Two of the three parameters of the unit cell, namely *a* and *c*, as well as the  $\beta$  angle, exhibit constant elongation (increase) as the temperature rises, whereas the parameter *b* decreases.

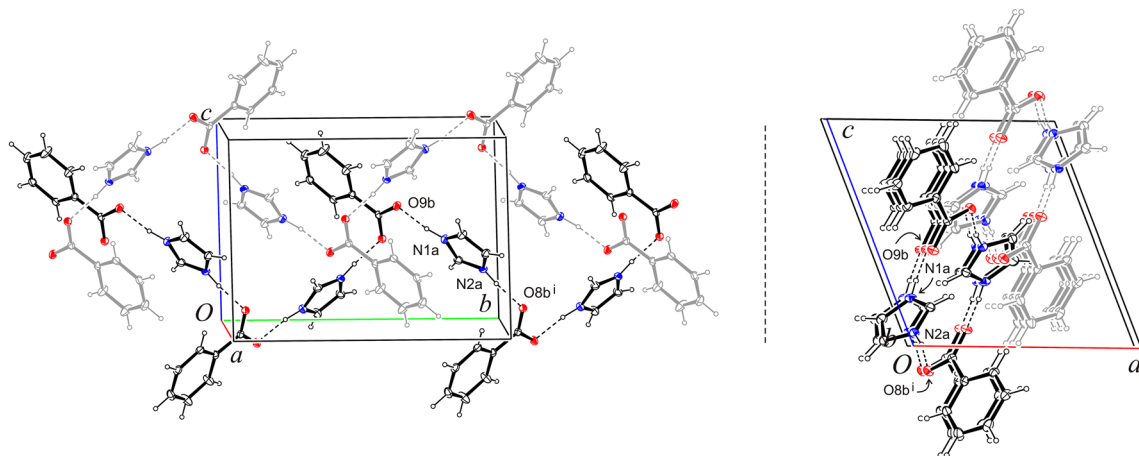


**Figure 1.** The helical structure in **BenImi** formed by cations and anions connected by  $\text{N}^+-\text{H}\cdots\text{O}^-$  hydrogen bonds.

Despite the different behavior of the parameters  $a$ ,  $c$  relative to  $b$ , the volume of the unit cell ( $V$ ) increases from 923.38(10) to 958.27(15) Å<sup>3</sup> with increasing temperature (from 100 to 300 K) (Table S5).

Positive temperature expansion of crystalline materials is a well-known physical phenomenon<sup>42</sup>. As the temperature increases, we observe an increase in the distance between atoms in the crystal. This behavior leads to an increase in the dimensions of the crystal on a macroscopic scale. The amplitude of temperature expansion depends on the type of interactions between molecules and the packing of the crystal lattice<sup>43</sup>. Anomalous temperature expansion in solids can be interpreted by analyzing the interactions between molecules or ions. It is most often explained by analyzing the strength of the interaction, the asymmetric shape of the potential energy curve, or structural distortions.

In the **BenImi** crystal lattice, ions interact with N<sup>+</sup>–H<sup>+</sup>⋯O<sup>-</sup> and C–H<sup>+</sup>⋯O hydrogen bonds. The donor–acceptor distances with temperature change (100/300 K) are 2.60/2.61 Å, 2.65/2.67 Å (for N<sup>+</sup>–H<sup>+</sup>⋯O<sup>-</sup>) and 3.20/3.19 Å (for C–H<sup>+</sup>⋯O). The following intermolecular hydrogen bonds were found: classical N1a–H1a⋯O9b and N2a–H2a⋯O8b<sup>i</sup> (within helices) and non-classical C1a–H1a⋯O9b hydrogen bonding (between helices) (Fig. S3). The geometrical parameters of hydrogen bonds: distance of donor hydrogen  $d_{D-H}$ , hydrogen-acceptor  $d_{H-A}$ , donor–acceptor  $d_{D-A}$ , and hydrogen bond angle  $\angle D-H\cdots A$  are summarized in Tables S3 and S4.

Calculations were performed using the quantum theory of atoms in molecules (QTAIM)<sup>44</sup> and Espinosa's approximation ( $E_{HB} \sim 1/2 V_{BCP}$ )<sup>45</sup> to determine the hydrogen bonding energies (Fig. S4, Tables S6 and S7). The  $V_{BCP}$  is the potential electron energy density at the bond critical point (BCP). The growth of electron density at the BCP is related to the increase in hydrogen bond strength. Bond critical points (BCPs) occur for hydrogen bonds: N1a–H1a⋯O9b, N2a–H2a⋯O8b<sup>i</sup>, and C1a–H1a⋯O9b. Intermolecular hydrogen bonds N1a–H1a⋯O9b and N2a–H2a⋯O8b<sup>i</sup> are  $E_{HB} = -16.88$  kcal·mol<sup>-1</sup> and  $-17.18$  kcal·mol<sup>-1</sup>, respectively; they are medium strength. Unconventional hydrogen bond C1a–H1a⋯O9b is  $E_{HB} = -1.82$  kcal·mol<sup>-1</sup>; it is weak strength. It shows that interactions within a helix are stronger than between helices in the salt under study.

Most compounds in the solid phase expand during heating<sup>1,2</sup> and pressure reduction<sup>34</sup>. A positive coefficient of temperature expansion and a positive coefficient of volume compressibility characterizes them. With decreasing temperature/increasing pressure, it is possible to observe the geometric contraction of certain compounds<sup>2,17</sup>. We can divide temperature/pressure expansion into volumetric and linear expansion. In the first case, we are talking about the change in volume as a function of temperature/pressure. In the second, we are talking about the change in length; in the direction of the principal axes X1, X2, and X3<sup>13</sup>. The coefficients of volumetric ( $\alpha_V$ ,  $K_V$ ) and linear ( $\alpha_L$ ,  $K_L$ ) thermal expansion ( $\alpha$ ) and compressibility ( $K$ ) are determined from the Eqs. (1) and (2), respectively<sup>1,10</sup>:

$$\alpha_V = \frac{\Delta V}{V} \frac{1}{\Delta T}, \quad K_V = -\frac{1}{V} \cdot \frac{\Delta V}{\Delta p}, \quad (1)$$

$$\alpha_L = \frac{\Delta l}{l} \frac{1}{\Delta T}, \quad K_L = -\frac{1}{l} \cdot \frac{\Delta l}{\Delta p} \quad (2)$$

where:  $\Delta V$ —change in volume of the crystal,  $\Delta T$ —change in temperature,  $\Delta p$ —change in pressure, and  $\Delta l$ —change in length in the X1, X2, or X3 direction.

As the temperature decreases, the values of the parameters  $a$ ,  $c$ , and  $V$  for imidazolium benzoate get smaller while the parameter  $b$  increases (Fig. 2, Table S1). The salt behaves similarly with increasing hydrostatic pressure (Fig. 2, Table S2).

Using the PASCAL program<sup>46</sup>, the principal axes were determined for temperature changes: X1<sub>T</sub> [0, -1, 0], X2<sub>T</sub> [0.7488, 0, 0.6628], and X3<sub>T</sub> [-0.6838, 0, 0.7297]. For pressure changes, the following orthogonal set of axes is X1<sub>p</sub> [-0.4688, 0, 0.8833], X2<sub>p</sub> [0.8226, 0, 0.5687], and X3<sub>p</sub> [0, -1, 0] (see Fig. 3). The directions X1<sub>T</sub>, X2<sub>T</sub>, and X3<sub>T</sub> correspond to X3<sub>p</sub>, X2<sub>p</sub>, and X1<sub>p</sub>, respectively. The coefficients of linear temperature expansion are equal to: -54.6(2), 47.8(8) and 193.2(5) 10<sup>-6</sup>·K<sup>-1</sup> for the X1<sub>T</sub>, X2<sub>T</sub> and X3<sub>T</sub> principal directions. The coefficient of volumetric temperature expansion is equal to 187.7(2) 10<sup>-6</sup>·K<sup>-1</sup>. The coefficients of linear compressibility are equal to 25.2(9), 12.2(7), and -4.2(6) TPa<sup>-1</sup>. The volumetric compressibility coefficient equals 55.4(8) TPa<sup>-1</sup>.

The value of the above coefficients of temperature expansion and compressibility shows that **BenImi** has positive and negative linear temperature expansion and positive volumetric temperature expansion, and positive volume compressibility (Fig. 3). We observe negative temperature expansion and negative compressibility in the X1<sub>T</sub> and X3<sub>p</sub> axis and positive temperature expansion and positive linear compressibility in the X2<sub>T</sub>, X3<sub>T</sub>, X1<sub>p</sub>, and X2<sub>p</sub>.

Analysis of the linear temperature expansion in **BenImi** showed that the interatomic distances along the X2<sub>T</sub> [0.7488, 0, 0.6628] and X3<sub>T</sub> [-0.6838, 0, 0.7297] shorten upon decreasing temperature. Changes in X2 directions are mainly related to C–H<sup>+</sup>⋯O hydrogen bonds, and in X3, related to changes in the strength of C–H<sup>+</sup>⋯π interactions. The elongation of interatomic distances in the X1 [0, -1, 0] direction is predominantly related to the  $b$  parameter of the unit cell. This direction is parallel to the helical chains formed by cations and anions connected by hydrogen bonds N<sup>+</sup>–H<sup>+</sup>⋯O<sup>-</sup>. With decreasing temperature/increasing pressure, the distances between ions in the X1<sub>T</sub>, X3<sub>p</sub> direction increase while leading to an decrease in the distance between molecules along the X2<sub>T</sub>, X2<sub>p</sub> and X3<sub>T</sub>, X1<sub>p</sub> directions. Based on the structural data analysis, it could be concluded that the imidazolium ion performs a librational motion, which leads to an increase in the distance between the ions (X1<sub>T</sub>/X3<sub>p</sub> direction).

As temperature and pressure change in the **BenImi** crystal structure, the relative arrangement of molecules changes. The angle between the anion and cation plane ( $\theta$ ) at 300 K equals 65.4°, and for 100 K, it is 60.7°. At 0.25 GPa, it is 63.5°, and at 3.41 GPa, it is 49.2°. The angle  $\theta$  decreases with decreasing temperature and increasing pressure (Fig. S5). The dihedral angle between the carboxylate group and the phenyl ring changes with

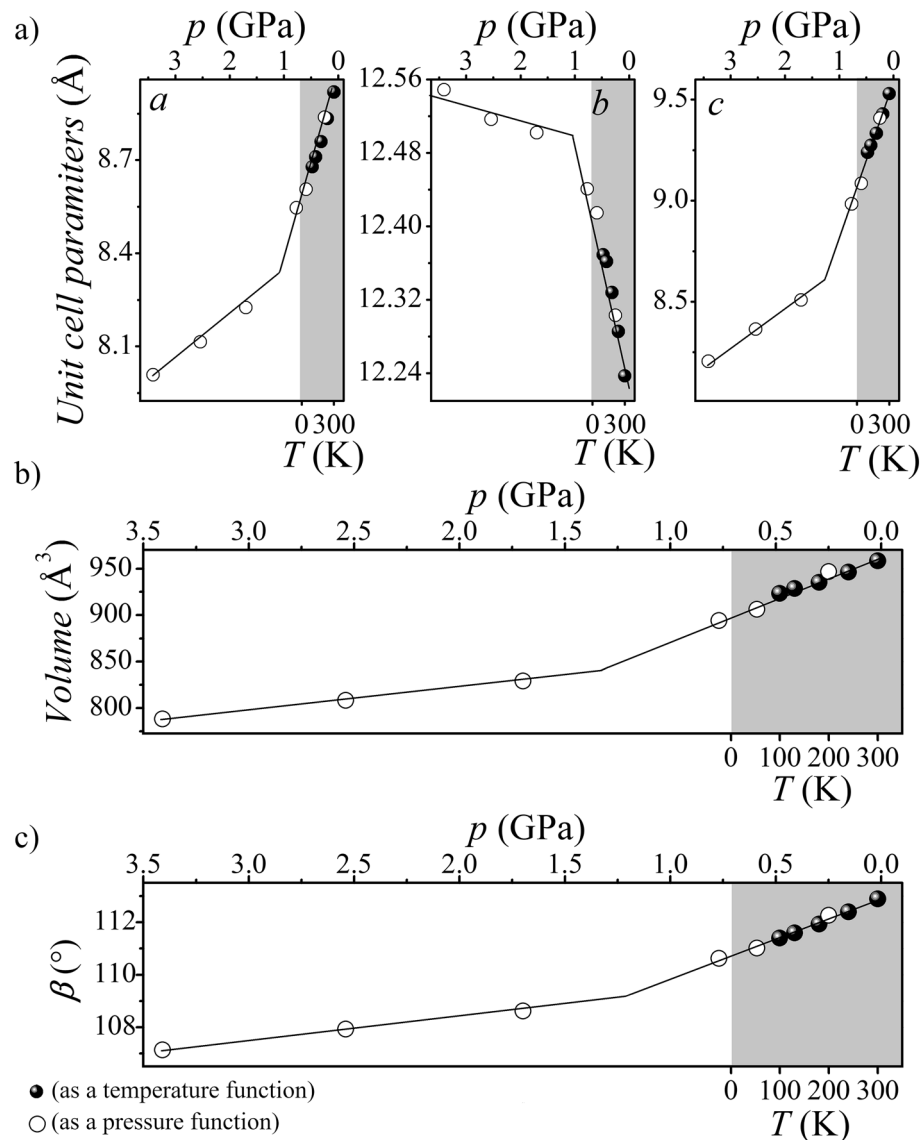


**Figure 2.** Temperature and pressure dependence of unit cell parameters  $a$ ,  $b$ , and  $c$  (a), unit cell volume  $V$  (b), and angle  $\beta$  (c) determined for BenImi.

temperature. At 100 K, this angle equals 7.59°, and at 300 K, it is 9.16°. The change in this angle is also observed in the pressure function. At 0.15 GPa, it is 8.23°, and at 3.41 GPa, it is 7.25°. The phenyl ring is twisted relative to the carboxylate groups, indicating that the carboxylate groups are rotated with the change in temperature and pressure. It was also observed that as the crystal temperature decreases, the distance between acid anions in BenImi increases. The C7a–C9a–N1b–C1b dihedral angle also changes from 18.18° (300 K) to 15.50° (100 K) and from 18.19° (0.25 GPa) to 13.42° (3.41 GPa). The observed changes indicate the rotation of the imidazole ion around the axis, passing through the carbon atoms of the five-membered ring (Fig. S6). Hence, it is to be expected that the librational motion of the imidazole ion affects the dynamics in the transverse direction of hydrogen bonds.

Network vibrations (phonons) significantly affect temperature expansion, especially at low temperatures<sup>2</sup>. When increasing the temperature, longitudinal vibrations lead to an increase in the size of the crystal<sup>22</sup>. Transverse vibrations may cause crystal size reduction with increasing temperature<sup>1,22</sup>. In a helical system, hydrogen bond shortening induced by transverse vibrations can lead to the elongation of the helix and its constriction in the direction perpendicular to its axis<sup>13,33</sup>. Transverse vibrations can be a source of NTE, especially at low temperatures<sup>1,2</sup>.

The helix pitch value ( $Sh_h$ ) was determined along the  $b$  direction, which is associated with negative temperature expansion (see Fig. 2a). The  $c$  and  $a$  directions, associated with positive temperature expansion (Fig. 2a), were associated with the semi-major axis ( $a_h$ ) and semi-minor axis ( $b_h$ ) of the ellipse, respectively. For the BenIm salt, an analysis of temperature- and pressure-induced changes in helix parameters was carried out (Fig. 4, Table S8). With decreasing temperature/increasing pressure, there is an increase in the value of the helix pitch and a decrease in the value of the semi-major axis. In addition, we observe an increase in the value of the

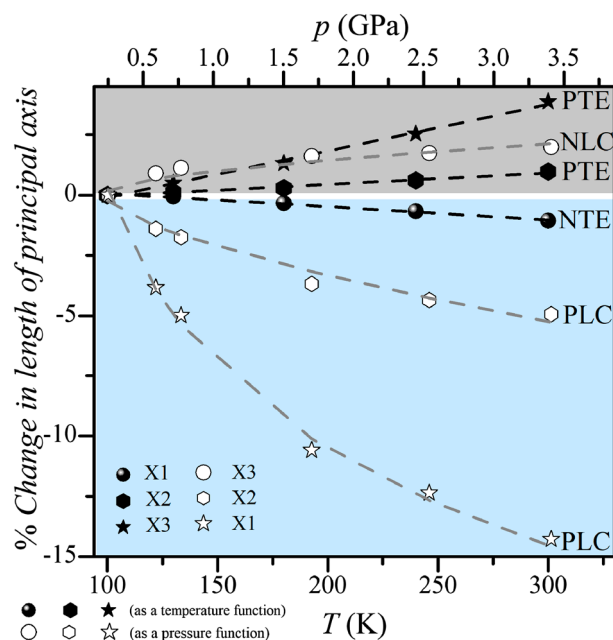


**Figure 3.** Relative changes in principal axes lengths as a function of temperature and pressure. *PTE* positive temperature expansion, *NTE* negative temperature expansion, *PLC* positive linear compressibility, *NLC* negative linear compressibility.

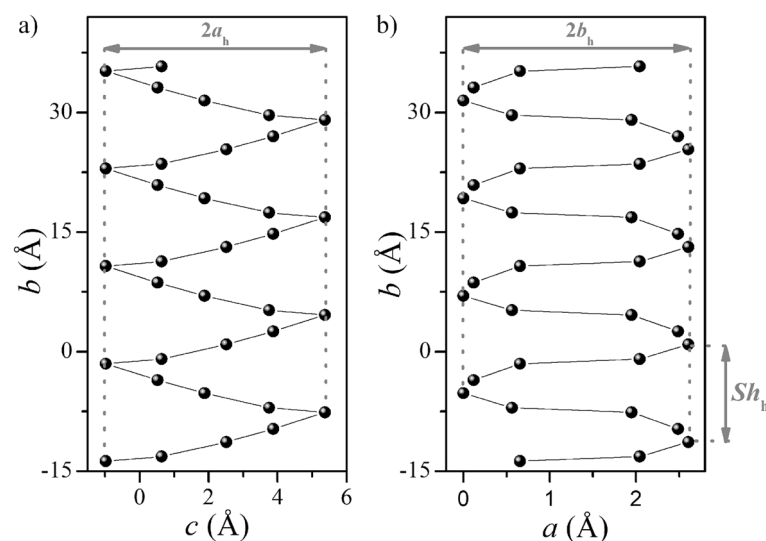


**Figure 4.** Projection on the *cb* (a) and *ab* (b) planes of the helix formed in the **BenImi** crystal structure at 300 K.  $Sh_h$  helix pitch,  $a_h$  semi-major axis,  $b_h$  semi-minor axis.

semi-minor axis with decreasing temperature/increasing pressure. The total temperature-dependent change in the parameter  $a$  of an elementary cell is affected by changes in the semi-minor axis ( $b_h$ ) and changes in the distance between the helices (see Fig. S7).

In **BenImi**, a helical model can explain anomalous temperature and pressure expansion. As the temperature decreases, the semi-major axis value decreases while the helix pitch and semi-minor axis increase (Fig. 5). The decrease in the value of the semi-minor axis and the increase in the helix pitch with decreasing temperature/increasing pressure is a consequence of changes in the structure of the  $N^+-H\cdots O^-$  hydrogen bond network and the libration motion of imidazolium ions (Fig. S8). Imidazole ions rotate around an axis passing through C2–C3 carbon atoms. In addition to changes in helix parameters, the angle between the carboxylate group and the phenyl ring also changes (Fig. S8). It shows that the system moving to a lower energy structure “makes changes” not only in the dimensions of the helix itself but also in its internal structure.

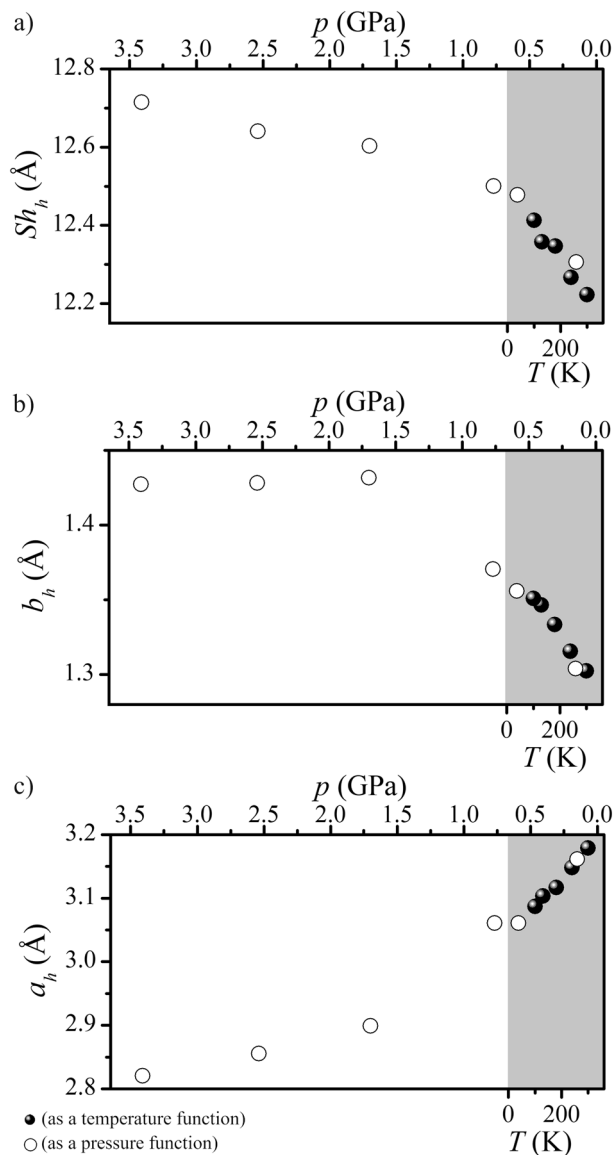


**Figure 5.** Dependence as a function of temperature and pressure of the helix pitch (a), the semi-minor axis (b), and the semi-major axis value (c).

We can study the dynamics of hydrogen bond networks using absorption spectra and Raman scattering methods<sup>47–49</sup>. Bands below  $200\text{ cm}^{-1}$  are associated with translational and librational network modes of the **BenImi** salt (Fig. 6). According to the X-Ray data, the lattice modes necessarily include the  $\text{N}^+ - \text{H} \cdots \text{O}^-$  hydrogen bonds motions. Two features at about  $160$  and  $100\text{ cm}^{-1}$  are related to hydrogen-bond stretching vibrations, and the other at about  $50\text{ cm}^{-1}$  is the twisting vibrations<sup>47–50</sup>. As the pressure increases, the bands observed at about  $160$  and  $100\text{ cm}^{-1}$  shift toward higher wavenumbers, indicating a shortening of hydrogen bond lengths, which is consistent with the results of the structural data (see Table S4).

Table S4 shows that as the pressure increases, the hydrogen bond angle of  $\text{N}^+ - \text{H} \cdots \text{O}^-$  decreases. The dependence of the  $1385\text{ cm}^{-1}$  band, related to  $\nu_{\text{sym}}(\text{COO}^-)$ <sup>37</sup>, observed in the mid-infrared spectrum as a function of hydrostatic pressure (see Fig. 7) is consistent with these data. This band, observed in the absorption spectrum, is associated with the bending of the hydrogen bridge of  $\text{N}^+ - \text{H} \cdots \text{O}^-$ . In addition, spectroscopic studies revealed an anomaly within the  $1\text{--}2\text{ GPa}$  region, confirming its occurrence in structural studies as a function of pressure (Fig. 7).

From infrared spectroscopy studies, we can also determine whether the lattice vibrations involving the hydrogen bond network are harmonic or anharmonic<sup>51,52</sup>. It is possible by analyzing the absorption band's shape associated with the hydrogen bridges' transverse vibrations<sup>51</sup>. In the case of anharmonic behavior, the band is asymmetric in which one slope is distinguished by a gentler slope directed toward a smaller value of the wavenumber (so-called “hard”) or a larger value of the wavenumber (so-called “soft”). The band is symmetric for harmonic behavior. We can describe the bands with parameters such as the damping parameter  $\Delta\nu/\nu_0$  and the

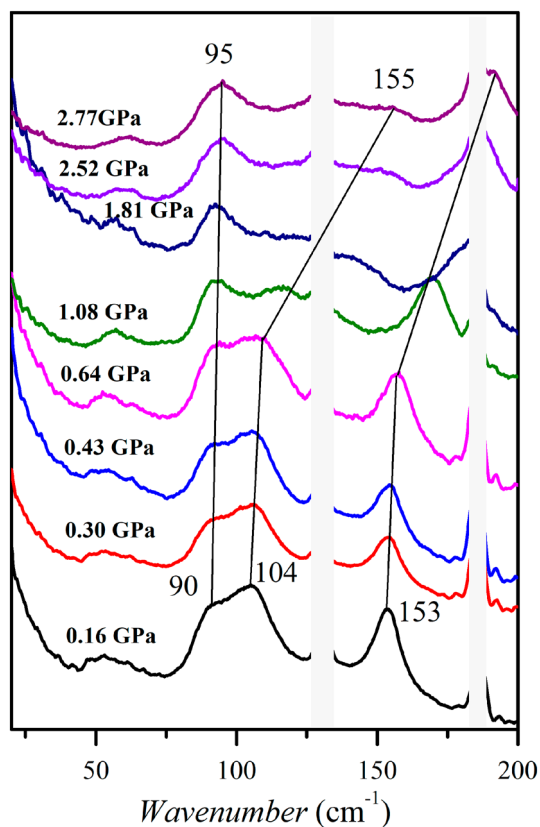


**Figure 6.** Raman spectrum of the **BenImi** salt as a function of hydrostatic pressure.

anharmonicity factor  $\Psi(A)^{51}$ . We can calculate the anharmonicity factor using the determined value of  $a$  and  $b$  (see insert in Fig. 8a):

$$\Psi(A) = 1 + \frac{1}{\pi} \left[ 1 - \left( \frac{b}{a} \right) \right], \quad \text{“for hard”}, \quad (3)$$

$$\Psi(A) = 1 - \frac{1}{\pi} \left[ 1 - \left( \frac{b}{a} \right) \right], \quad \text{“for soft”}. \quad (4)$$

Figure 8 shows the infrared spectra of **BenImi** salts recorded at 290, 230, 150, 70, and 10 K. The band near  $870 \text{ cm}^{-1}$  is associated with deformation vibrations of the N–H bond in the  $\text{N}^+ \cdots \text{H} \cdots \text{O}^-$  hydrogen bond<sup>37</sup>. As the temperature decreases, the intensity of the band increases, and its bandwidth decreases (Fig. 8c). Analysis of the band shape showed that it is characterized by “soft” ( $a < b$ ) anharmonicity<sup>51</sup>. Figure 8b shows the dependence of the anharmonicity coefficient for **BenImi** as a function of temperature. A value of this coefficient greater than 1 introduces a negative contribution to the Grüneisen function, which leads to negative thermal expansion<sup>51,52</sup>.

## Conclusions

We have proposed a helical model to explain the negative linear thermal expansion and compression of imidazolium benzoate crystals. The mechanism of the negative linear behavior can be correlated with the structural distortions of helices. As the temperature drops and the hydrostatic pressure rises, the values of the parameters  $a$ ,  $c$ , and  $V$  decrease while the value of parameter  $b$  rises. In the crystal lattice, ions interact by conventional  $\text{N}^+ \cdots \text{H} \cdots \text{O}^-$  (within helices; medium strength) and unconventional  $\text{C} \cdots \text{H} \cdots \text{O}$  (between helices; weak strength) hydrogen bonds. The interactions within the helix are stronger than interactions between helices. In a helical system with decreasing temperature and increasing pressure, the helix pitch increases while the value of the semi-major axis decreases. It leads to the elongation and contraction of the helix along its axis and in the perpendicular direction, respectively. These NLE and NLC effects have been correlated with the internal structure of the helix, involving the rotations of the imidazolium ions and rearrangements of the carboxylate groups.

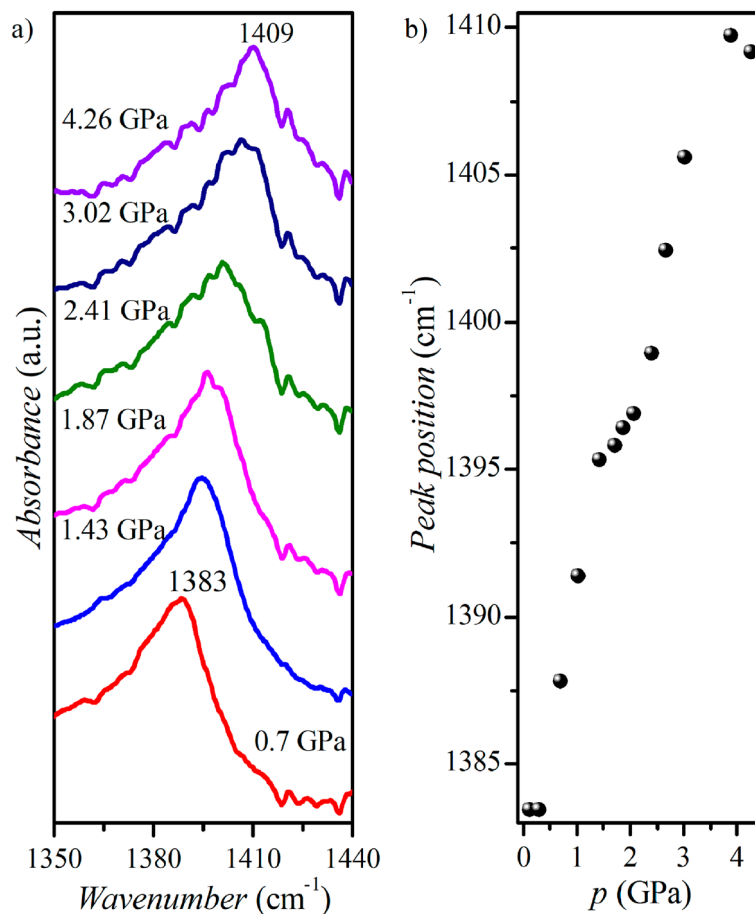


**Figure 7.** Absorbance spectrum of **BenImi** salt as a function of hydrostatic pressure (left) and the dependence of the position of the 1385  $\text{cm}^{-1}$  band as a function of pressure (right).

## Methods

Imidazole benzoate salt (**BenImi**) was obtained by reacting benzoic acid with imidazole in the organic solvent ethyl acetate (99.8% purity, Merc KGaA)<sup>37</sup>. The substrates were weighed in a molar ratio 1:1. Each substrate was independently dissolved in ethyl acetate. Then the imidazole solution was added to the acid solution and stirred using a magnetic stirrer. The resulting white salt precipitate was drained on a Buchner funnel and washed with ethyl acetate to remove unreacted substrates.

Crystals of imidazolium benzoate (**BenImi**) suitable for single-crystal X-ray diffraction analysis were obtained by slow evaporation from solvent in ethyl acetate. X-ray diffraction measurements were carried out at 100, 130<sup>37</sup>, 180, 240, and 300 K on a SuperNova Dual Atlas diffractometer using Mo  $K\alpha$  radiation ( $\lambda = 0.71073 \text{ \AA}$ )<sup>53</sup> (Table S1). The crystal structure was solved by the dual-space direct methods algorithm (SHELXT<sup>54–56</sup>) and refined against  $F^2$  using all data (SHELXL<sup>55–57</sup>). The positions of the H atoms bonded to the N atoms were obtained from difference Fourier maps and were refined freely with isotropic displacement parameters. The remaining H atoms were placed geometrically at calculated positions and refined using the riding model, with C–H = 0.95  $\text{\AA}$  ( $Csp^2H$ ) for 100, 130<sup>37</sup>, 180 K or with C–H = 0.94 and 0.93  $\text{\AA}$  ( $Csp^2H$ ) for 240 and 300 K, respectively and  $U_{iso}(H) = 1.2U_{eq}(C)$  for all measurement temperatures. The crystallographic data are available from the Cambridge Crystallographic Database Centre (CCDC 2265522 (100 K), CCDC 1892005 (130 K)<sup>37</sup>, 2265523 (180 K), 2265524 (240 K), 2265525 (300 K)). Molecular illustrations were prepared using ORTEP-3 for Windows<sup>56</sup>. The material for publication was prepared using WINGX<sup>56</sup> and PLATON<sup>58</sup>.

High-pressure experiments were carried out with a modified Merrill–Bassett diamond-anvil cell (DAC)<sup>59</sup>. The pressure in the DAC chamber was calibrated by the ruby fluorescence with a Photon Control spectrometer, affording an accuracy of 0.02 GPa<sup>60</sup>. A good quality single crystal was placed in the DAC chamber with several ruby chips and the Daphne oil 7575 was used as the pressure-transmitting medium<sup>61</sup>. The pressure was gradually increased and several X-ray diffraction data sets were collected up to 3.41 GPa on a 4-cycle Excalibur EOS diffractometer ( $\lambda_{MoK\alpha} = 0.71073 \text{ \AA}$ ). Preliminary data reduction were performed with the CrysAlis software from Oxford Diffraction. The crystal structures of **BenImi** under high-pressure were solved by direct methods<sup>54</sup> and refined by full-matrix least squares on  $F^2$ <sup>57</sup>. The detail crystal data of high-pressure measurements are listed in Table S2 and also deposited in the CIF format with numbers CCDC 2263553–2263558.



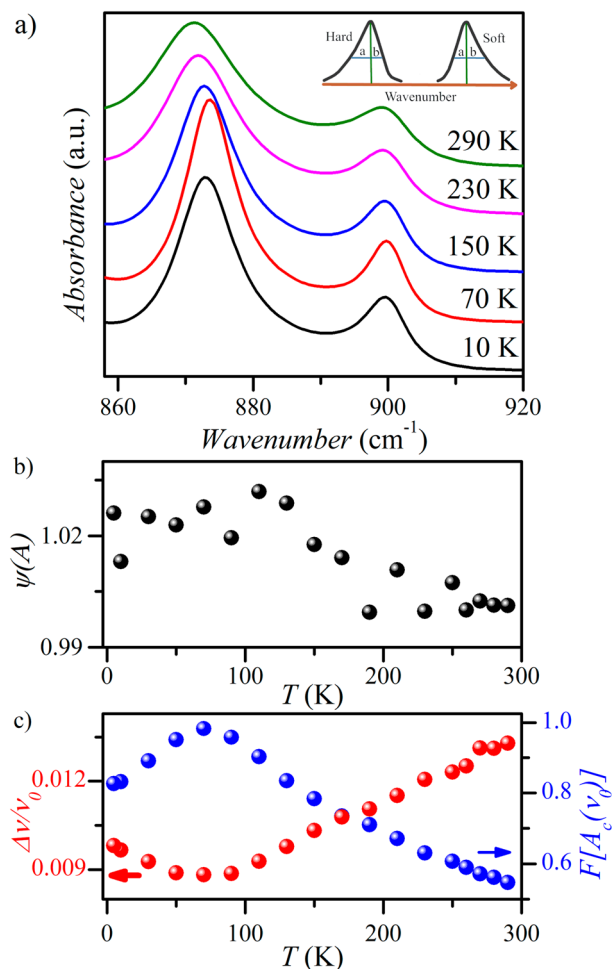


**Figure 8.** Infrared spectra of BenImi salt (a); anharmonicity coefficient (b), attenuation coefficient, and band intensity as a function of temperature (c).

Absorption spectra in the KBr matrix ( $c = 1:500$ ), in the mid-infrared range ( $650\text{--}4000\text{ cm}^{-1}$ ), were recorded on a Bruker Equinox 55 FT-IR spectrometer coupled to a Hyperion 2000 microscope. They were recorded with a spectral resolution of  $2\text{ cm}^{-1}$ . A tungsten lamp was used as the radiation source. DLATGS ( $400\text{--}7000\text{ cm}^{-1}$ ) and liquid nitrogen-cooled MCT ( $500\text{--}7000\text{ cm}^{-1}$ ) detectors were used. KBrGe was used as a beamsplitter. Studies of spectroscopic properties as a function of temperature were carried out using cryostats: Oxford Inst. CF 2102 (from 5 to 300 K) and Linkam THMS 600 (from 273 to 600 K). Infrared spectra as a function of pressure were recorded for **BenImi** using a Merrill–Bessett high-pressure chamber. Gasket Stainless was used as seals between the diamonds. Potassium bromide (BeCu) was used as a medium to transfer hydrostatic pressure from the anvil pistons to the sample. Ruby crystals were used to determine the value of the applied pressure. Type IIa diamonds (culet size— $0.8\text{ mm}$ ) embedded in anvil rings of BeCu were used.

Raman spectra were recorded on a LabRAM HR 800 UV HORIBA Jobin Yvon spectrometer, which is equipped with a liquid nitrogen-cooled CCD detector. The spectrum was recorded using He–Ne laser excitation ( $\lambda = 632.8\text{ nm}$ ) with a spectral resolution better than  $2\text{ cm}^{-1}$ . The laser power on the sample was less than  $1\text{ mW}$ . Raman spectra of **BenImi** were recorded in the spectral range from  $50$  to  $3250\text{ cm}^{-1}$  using a  $50\times$  objective. Raman spectra as a function of pressure were recorded using a Diacell<sup>®</sup> CryoDAC-Mega diamond anvil. Cesium iodide (CsI) was used as a medium to transfer hydrostatic pressure from the anvil pistons to the sample; gasket of stainless steel were used. Ruby crystals were used to determine the value of the applied pressure. Type Ia diamonds (culet size— $0.7\text{ mm}$ ) were embedded in BeCu anvil rings.

### Data availability

All data generated or analysed during this study are included in this published article (and its Supplementary Information files). The detail crystal data of low-temperature and high-pressure measurements are deposited in the CIF format, available free of charge on request from Cambridge Crystallographic Database Centre at <https://www.ccdc.cam.ac.uk/structures/> with numbers: 1892005, 2265522–2265525 (low-temperature) and 2263553–2263558 (high-pressure).

Received: 21 August 2023; Accepted: 9 October 2023

Published online: 13 October 2023

## References

- Miller, W., Smith, C. W., Mackenzie, D. S. & Evans, K. E. Negative thermal expansion: A review. *J. Mater. Sci.* **44**, 5441–5451 (2009).
- Barrera, G. D., Bruno, J. A. O., Barron, T. H. & Allan, N. L. Negative thermal expansion. *J. Phys. Condens. Matter* **17**, R217–R252 (2005).
- Evans, J. S. O. Negative thermal expansion materials. *J. Chem. Soc. Dalton Trans.* **19**, 3317–3326 (1999).
- Cairns, A. B. & Goodwin, A. L. Negative linear compressibility. *Phys. Chem. Chem. Phys.* **17**, 20449–20465 (2015).
- Zieliński, W. & Katrusiak, A. Hydrogen bonds NH $\cdots$ N in compressed benzimidazole polymorphs. *Cryst. Growth Des.* **13**, 696–700 (2013).
- Goodwin, A. L. *et al.* Colossal positive and negative thermal expansion in the framework material Ag<sub>3</sub>[Co(CN)<sub>6</sub>]. *Science* **319**, 794–797 (2008).
- Ogborn, J. M., Collings, I. E., Moggach, S. A., Thompson, A. L. & Goodwin, A. L. Supramolecular mechanics in a metal-organic framework. *Chem. Sci.* **3**, 3011–3017 (2012).
- Lind, C. Two decades of negative thermal expansion research: Where do we stand?. *Materials* **5**, 1125–1154 (2012).
- Sleight, A. W. *Negative thermal expansion material*. Patent US5322559A (Oregon State University, 1994).
- Bhattacharya, S. & Saha, B. K. Uniaxial negative thermal expansion in an organic complex caused by sliding of layers. *Cryst. Growth Des.* **12**, 4716–4719 (2012).
- Engel, E. R., Smith, V. J., Bezuidenhout, C. X. & Barbour, L. J. Uniaxial negative thermal expansion facilitated by weak host–guest interactions. *Chem. Commun.* **50**, 4238–4241 (2014).
- Birkedal, H., Schwarzenbach, D. & Pattison, P. Observation of uniaxial negative thermal expansion in an organic crystal. *Angew. Chem. Int. Ed. Engl.* **41**, 754–756 (2002).
- Das, D., Jacobs, T. & Barbour, L. J. Exceptionally large positive and negative anisotropic thermal expansion of an organic crystalline material. *Nat. Mater.* **9**, 36–39 (2010).
- Takahashi, H. & Tamura, R. Low temperature phase transition induced biaxial negative thermal expansion of 2,4-dinitroanisole. *CrystEngComm* **17**, 8888–8896 (2015).
- Marinkovic, B. A. *et al.* Correlation between AO<sub>6</sub> polyhedral distortion and negative thermal expansion in orthorhombic Y<sub>2</sub>Mo<sub>3</sub>O<sub>12</sub> and related materials. *Chem. Mater.* **21**, 2886–2894 (2009).
- Goodwin, A. L. & Kepert, C. J. Negative thermal expansion and low-frequency modes in cyanide-bridged framework materials. *Phys. Rev. B* **71**, 140301(R) (2005).
- Salvador, J. R., Guo, F., Hogan, T. & Kanatzidis, M. G. Zero thermal expansion in YbGaGe due to an electronic valence transition. *Nature* **425**, 702–705 (2003).
- Hu, P. *et al.* Zero thermal expansion in (1–x)PbTiO<sub>3</sub>–xBi(Mg, Ti)<sub>1/2</sub>O<sub>3</sub> piezoceramics. *J. Mater. Chem.* **19**, 1648–1652 (2009).
- Zięba, S., Gzella, A., Dubis, A. T. & Łapiński, A. Combination of negative, positive, and near-zero thermal expansion in bis(imidazolium) terephthalate with a helical hydrogen-bonded network. *Cryst. Growth Des.* **21**, 3838–3849 (2021).
- Lama, P., Das, R. K., Smith, V. J. & Barbour, L. J. A combined stretching–tilting mechanism produces negative, zero and positive linear thermal expansion in a semi-flexible Cd(II)-MOF. *Chem. Commun.* **50**, 6464–6467 (2014).
- Henke, S., Schneemann, A. & Fischer, R. A. Massive anisotropic thermal expansion and thermo-responsive breathing in metal-organic frameworks modulated by linker functionalization. *Adv. Funct. Mater.* **23**, 5990–5996 (2013).
- Bhattacharya, S., Saraswatula, V. G. & Saha, B. K. Thermal expansion in alkane diacids—Another property showing alternation in an odd-even series. *Cryst. Growth Des.* **13**, 3651–3656 (2013).
- Mary, T. A., Evans, J. S. O., Vogt, T. & Sleight, A. W. Negative thermal expansion from 0.3 to 1050 Kelvin in ZrW<sub>2</sub>O<sub>8</sub>. *Science* **272**, 90–92 (1996).
- Dwivedi, B., Shrivastava, A., Negi, L. & Das, D. Colossal positive and negative axial thermal expansion induced by scissor-like motion of a two-dimensional hydrogen bonded network in an organic salt. *Cryst. Growth Des.* **19**, 2519–2524 (2019).
- Lama, P., Hazra, A. & Barbour, L. J. Accordion and layer-sliding motion to produce anomalous thermal expansion behaviour in 2D-coordination polymers. *Chem. Commun.* **55**, 12048–12051 (2019).
- Shrivastava, A., Negi, L. & Das, D. Area negative thermal expansion in a mixed metal mixed organic MOF: Elevator-platform mechanism induced by O–H $\cdots$ O hydrogen bonding. *CrystEngComm* **20**, 4719–4723 (2018).
- Ding, X., Unruh, D. K., Groeneman, R. H. & Hutchins, K. M. Controlling thermal expansion within mixed cocrystals by tuning molecular motion capability. *Chem. Sci.* **11**, 7701–7707 (2020).
- Anderson, P. W. & Blount, E. I. Symmetry considerations on martensitic transformations: “Ferroelectric” metals?. *Phys. Rev. Lett.* **14**, 217–219 (1965).
- Fradkin, M. A. The effect of strain on the thermodynamics of the weakly first-order phase transition. *J. Phys. Condens. Matter* **9**, 7925–7932 (1997).
- Hausühl, S., Bohaty, L. & Becker, P. Piezoelectric and elastic properties of the nonlinear optical material bismuth triborate, Bi<sub>3</sub>O<sub>6</sub>. *Appl. Phys. A* **82**, 495–502 (2006).
- Prawer, S., Smith, T. F. & Finlayson, T. R. The room temperature elastic behaviour of CsH<sub>2</sub>PO<sub>4</sub>. *Aust. J. Phys.* **38**, 63–84 (1985).
- Keller, R., Holzapfel, W. B. & Schulz, H. Effect of pressure on the atom positions in Se and Te. *Phys. Rev. B* **16**, 4404–4412 (1977).
- Saha, B. K. Thermal expansion in organic crystals. *J. Indian Inst. Sci.* **97**, 177–191 (2017).
- Kaźmierczak, M., Patyk-Kaźmierczak, E. & Katrusiak, A. Compression and thermal expansion in organic and metal-organic crystals: The pressure-temperature correspondence rule. *Cryst. Growth Des.* **21**, 2196–2204 (2021).
- Hazen, R. M. & Finger, L. W. Comparative crystal chemistry: Temperature, pressure, composition and the variation of crystal structure. In *High-Pressure Researches in Geoscience* (ed. Schreyer, W.) 151–176 (Schweizerbart Science Publishers, 1982).
- Zięba, S. *et al.* Effect of counter ions on physical properties of imidazole-based proton conductors. *Electrochim. Acta* **306**, 575–589 (2019).
- Zięba, S. *et al.* Toward a new type of proton conductor based on imidazole and aromatic acids. *Phys. Chem. Chem. Phys.* **21**, 17152–17162 (2019).
- Mohamed, S., Tocher, D. A., Vickers, M., Karamertzanis, P. G. & Price, S. L. Salt or cocrystal? A new series of crystal structures formed from simple pyridines and carboxylic acids. *Cryst. Growth Des.* **9**, 2881–2889 (2009).
- Schmuck, C. Molecules with helical structure: How to build a molecular spiral staircase. *Angew. Chem. Int. Ed.* **42**, 2448–2452 (2003).
- Miyasaka, M., Pink, M., Rajca, S. & Rajca, A. Noncovalent interactions in the asymmetric synthesis of rigid, conjugated helical structures. *Angew. Chem. Int. Ed.* **121**, 6068–6071 (2009).
- Cornelissen, J. J. L. M., Rowan, A. E., Nolte, R. J. M. & Sommerdijk, N. A. J. M. Chiral architectures from macromolecular building blocks. *Chem. Rev.* **101**, 4039–4070 (2001).
- Barron, T. H. K. & White, G. K. *Heat Capacity and Thermal Expansion at Low Temperatures* (Springer, 1999).
- Sleight, A. W. Thermal contraction. *Endeavour* **19**, 64–68 (1995).
- Bader, R. F. W. *Atoms in Molecules, A Quantum Theory* (Oxford University Press, 1990).

45. Espinosa, E., Molins, E. & Lecomte, C. Hydrogen bond strengths revealed by topological analyses of experimentally observed electron densities. *Chem. Phys. Lett.* **285**, 170–173 (1998).
46. Cliffe, M. J. & Goodwin, A. L. PASCAL: A principal axis strain calculator for thermal expansion and compressibility determination. *J. Appl. Cryst.* **45**, 1321–1329 (2012).
47. Joesten, M. D. & Schaad, L. J. *Hydrogen Bond* (Marcel Dekker, 1974).
48. Schuster, P. et al. (eds) *The Hydrogen Bond* (North-Holland, 1976).
49. Hadži, D. *Theoretical Treatment of Hydrogen Bonding* (Wiley, 1997).
50. Widelicka, M., Pogorzelec-Glaser, K., Pankiewicz, R. & Łapiński, A. Spectroscopic investigations of the new anhydrous proton-conducting compound of pyrazole with oxalate acid. *J. Raman Spectrosc.* **50**, 1914–1925 (2019).
51. Plendl, J. N. & Mansur, L. C. Anomalous thermal expansion with infrared spectroscopy. *Appl. Opt.* **11**, 1194–1199 (1972).
52. Plendl, J. N. Some new interrelation in the properties of solids based on anharmonic cohesive forces. *Phys. Rev.* **123**, 1172–1180 (1961).
53. CrysAlis PRO. *Version 1.171.38.46, Rigaku Oxford Diffraction* (Yarnton, 2015).
54. Sheldrick, G. M. SHELXT—Integrated space-group and crystal-structure determination. *Acta Cryst.* **A71**, 3–8 (2015).
55. Dolomanov, O. V., Bourhis, L. J., Gildea, R. J., Howard, J. A. K. & Puschmann, H. OLEX2: A complete structure solution, refinement and analysis program. *J. Appl. Cryst.* **42**, 339–341 (2009).
56. Farrugia, L. J. WinGX and ORTEP for Windows: An update. *J. Appl. Cryst.* **45**, 849–854 (2012).
57. Sheldrick, G. M. Crystal structure refinement with SHELXL. *Acta Cryst.* **C71**, 3–8 (2015).
58. Spek, A. L. Structure validation in chemical crystallography. *Acta Cryst.* **D65**, 148–155 (2009).
59. Merrill, L. & Bassett, W. A. Miniature diamond anvil pressure cell for single crystal X-ray diffraction studies. *Rev. Sci. Instrum.* **45**, 290–294 (1974).
60. Piermarini, G. J., Block, S., Barnett, J. D. & Forman, R. A. Calibration of the pressure dependence of the  $R_1$  ruby fluorescence line to 195 Kbar. *J. Appl. Phys.* **46**, 2774–2780 (1975).
61. Staško, D., Prchal, J., Klicpera, M., Aoki, S. & Murata, K. Pressure media for high pressure experiments, Daphne Oil 7000 series. *High Pressure Res.* **40**, 525–536 (2020).

## Acknowledgements

The research was financed from budget funds for science in 2020–2023 as a research project under the “PREL-UDIUM-18” program (National Science Centre, Poland, 2019/35/N/ST5/03324) and supported by the Foundation for Polish Science (FNP) (START 098.2022).

## Author contributions

Conceptualization, S.Z., A.Ł.; data curation, S.Z., M.R.; formal analysis, S.Z., M.R., A.G., A.T.D.; funding acquisition, S.Z.; investigation, S.Z. M.R. A.K. A.G. A.T.D. A.Ł.; methodology, S.Z., A.T.D., A.Ł.; project administration, S.Z., A.Ł.; resources, S.Z. M.R. A.K. A.G. A.T.D. A.Ł.; supervision, A.K. A.G. A.T.D. A.Ł.; validation, A.K. A.G. A.T.D. A.Ł.; writing-original draft preparation, S.Z., A.Ł.; writing-review and editing, S.Z. M.R. A.K. A.G. A.T.D. A.Ł.; All authors read and approved the final manuscript.

## Competing interests

The authors declare no competing interests.

## Additional information

**Supplementary Information** The online version contains supplementary material available at <https://doi.org/10.1038/s41598-023-44467-y>.

**Correspondence** and requests for materials should be addressed to S.Z. or A.Ł.

**Reprints and permissions information** is available at [www.nature.com/reprints](http://www.nature.com/reprints).

**Publisher’s note** Springer Nature remains neutral with regard to jurisdictional claims in published maps and institutional affiliations.



**Open Access** This article is licensed under a Creative Commons Attribution 4.0 International License, which permits use, sharing, adaptation, distribution and reproduction in any medium or format, as long as you give appropriate credit to the original author(s) and the source, provide a link to the Creative Commons licence, and indicate if changes were made. The images or other third party material in this article are included in the article’s Creative Commons licence, unless indicated otherwise in a credit line to the material. If material is not included in the article’s Creative Commons licence and your intended use is not permitted by statutory regulation or exceeds the permitted use, you will need to obtain permission directly from the copyright holder. To view a copy of this licence, visit <http://creativecommons.org/licenses/by/4.0/>.

© The Author(s) 2023